arXiv:2503.09040v1 [cs.CV] 12 Mar 2025

Motion Blender Gaussian Splatting for Dynamic Reconstruction

Xinyu Zhang, Haonan Chang, Yuhan Liu, Abdeslam Boularias
Department of Computer Science, Rutgers University
{xz653, yl1834, hc856, ab1544}@rutgers.edu

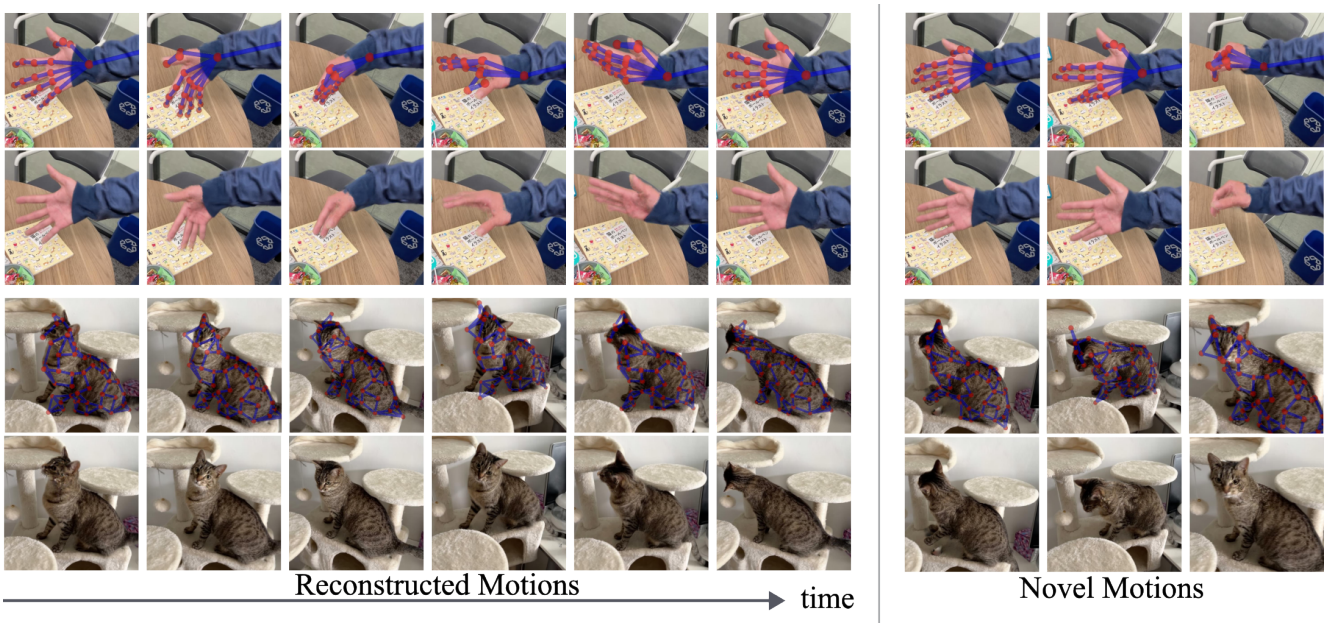


Figure 1. Our method reconstructs and renders dynamic scenes into 3D Gaussians and motion graphs from input videos. The learned motion graphs of a hand and a cat are visualized in the first and third rows. These graphs can be easily manipulated to create novel motions.

Abstract

Gaussian splatting has emerged as a powerful tool for high-fidelity reconstruction of dynamic scenes. However, existing methods primarily rely on implicit motion representations, such as encoding motions into neural networks or per-Gaussian parameters, which makes it difficult to further manipulate the reconstructed motions. This lack of explicit controllability limits existing methods to replaying recorded motions only, which hinders a wider application. To address this, we propose Motion Blender Gaussian Splatting (MB-GS), a novel framework that uses motion graph as an explicit and sparse motion representation. The motion of graph links is propagated to individual Gaussians via dual quaternion skinning, with learnable weight painting functions determining the influence of each link. The motion graphs and 3D Gaussians are jointly optimized from input videos via differentiable rendering. Experiments show that MB-GS achieves state-of-the-art performance on the iPhone dataset while being competitive on HyperNeRF. Additionally, we demonstrate the application potential of our method in generating novel object motions and robot demonstrations through motion editing. Video demonstrations can be found at mlzxy.github.io/mbgs.

1. Introduction

Reconstructing and modeling dynamic 3D scenes is a fundamental challenge in computer vision, with applications spanning content creation, robotics, and augmented reality. Recent work on 3D Gaussian splatting has made significant progress in capturing dynamic scenes, enabling efficient and high-fidelity reconstruction [12, 17, 24, 44, 46, 47, 49].

Existing Gaussian splatting-based methods utilize 3D Gaussians to represent geometry and appearance, paired with motion modules that determine the movements of Gaussians over time. For instance, 4DGaussians [46] and Deformable-GS [48] encode motion implicitly into neural networks. Shape-of-Motion [44] and STG [24] use shallower models that require dense per-Gaussian motion parameters. While these approaches achieve high-fidelity re-

construction of complex scenes, their implicit motion representation makes it difficult to manipulate the reconstructed motions. This lack of direct and explicit controllability restricts existing methods to replaying recorded motions only.

Therefore, a key question to answer is: can we develop an explicit and sparse motion representation without compromising the ability to reconstruct complex scenes? To answer this question, we revisit some classical animation techniques [13]. Explicit motion representations, such as deformation graphs [42], harmonic coordinates [15], and cage [30], have been developed to animate objects with diverse motions. However, these classical methods focus on applying manually designed motions to mesh surfaces instead of 3D Gaussians [5]. Further, these methods are not able to reconstruct motion or geometry from visual data.

Inspired by mesh animation techniques, we propose using kinematic trees and deformable graphs as motion representations for Gaussian splatting-based reconstruction. Kinematic trees are well-suited for capturing the motions of articulated objects, such as human bodies or robots, while deformable graphs, free from topological constraints, excel at modeling non-rigid object deformations. We collectively refer to kinematic trees and deformable graphs as motion graphs. Motions of graph links are propagated to individual Gaussians through dual quaternion skinning [16]. The influence of each graph link on a Gaussian is predicted by a learnable weight painting function. The graphs are initialized from point clouds and 2D keypoints at a canonical frame. Both the Gaussians and motion graphs are optimized end-to-end jointly from videos via differentiable rendering. We term our approach Motion Blender Gaussian Splatting (MB-GS). Our contributions can be summarized as follows.

- We introduce a dynamic Gaussian splatting framework based on explicit and sparse motion graphs. Gaussian motions are predicted by blending the link motions.
- We propose two types of parametric motion graphs—kinematic trees and deformable graphs—and a learnable weight painting function based on Gaussian kernels, along with optimization details in Sec. 3.4. Our method learns both 3D Gaussians and motion graphs jointly.
- Compared with state-of-the-art, our method outperforms Shape-of-Motion on the iPhone dataset [8], and achieves competitive performance with 4DGaussians on HyperNerf [32]. Further, we demonstrate the application potential of our approach on creating novel object motions and synthesizing robot demonstrations through motion editing. This can lead to significant efficiency improvement in gathering training datasets for robot learning [43].

2. Related Works

Dynamic Reconstruction. Dynamic reconstruction aims at recovering the geometry, appearance and motion of dynamic scenes from visual data [3, 4, 39, 52]. Early approaches, such as DynamicFusion [29] and SurfelWarp [9], rely on 3D representations like the truncated signed distance function (TSDF) or surfel [33], coupled with explicit deformation graphs to model motion. Recent advances have shifted toward using NeRF [1, 7, 28, 31, 32, 34] and 3D Gaussian [17, 24, 46, 47, 49] as 3D representations. Gaussian splatting-based methods, in particular, have gained rising attention due to their ability of high-quality reconstruction and real-time rendering. For example, 4DGaussians [46] and Deformable-GS [48] encode motion implicitly using deformation networks. Shape-of-Motion [44], GaussianFlow [25] and STG [24] employ shallower models, such as polynomials, which require dense per-Gaussian motion parameters. In contrast to these approaches, our method introduces a sparse and explicit graph-based motion representation for Gaussian splatting, which enables the reconstruction of realistic and complex scenes with greater interpretability and direct and explicit control of the animation.

Explicit Motion Representations. Explicit motion representations offer intuitive visualization and straightforward motion manipulation. Gaussian-based avatar modeling methods [22, 35, 50] rely on parametric human templates, such as SMPL [27], but are inherently limited to human subjects and cannot generalize to arbitrary dynamic objects. SC-GS [12] introduces sparse control points, which can be dragged to create new motions. But SC-GS is restricted to simple, synthetic scenes like those in D-NeRF [34]. CAMM [20] employs kinematic chains for motion representation but is limited to meshes instead of 3D Gaussians and requires occlusion-free videos with clean backgrounds. On the other hand, classical animation techniques [13] utilize explicit motion representations such as deformation graphs [42], harmonic coordinates [15], and cage [30]. However, these methods only focus on applying manually designed motions to mesh surfaces and are not designed for reconstructing motion or geometry from unstructured video data. In contrast, our method introduces a graph-based motion representation for Gaussian splatting, where motion is propagated from sparse graph links to individual Gaussians. 3D Gaussians and motion graphs are jointly optimized from videos of realistic and complex scenes.

3. Method

Sec. 3.1 introduces the overall motion blender framework for dynamic Gaussian splatting. Kinematic trees and deformable graphs, two types of motion graphs, are presented in Sec. 3.2. The weight painting function and the radiance Gaussian kernel are proposed in Sec. 3.3. Finally, the proposed optimization process is detailed in Sec. 3.4.

Preliminaries. Gaussian splatting represents a static 3D scene explicitly with a set $\mathcal{G}$ of 3D Gaussians. Each 3D

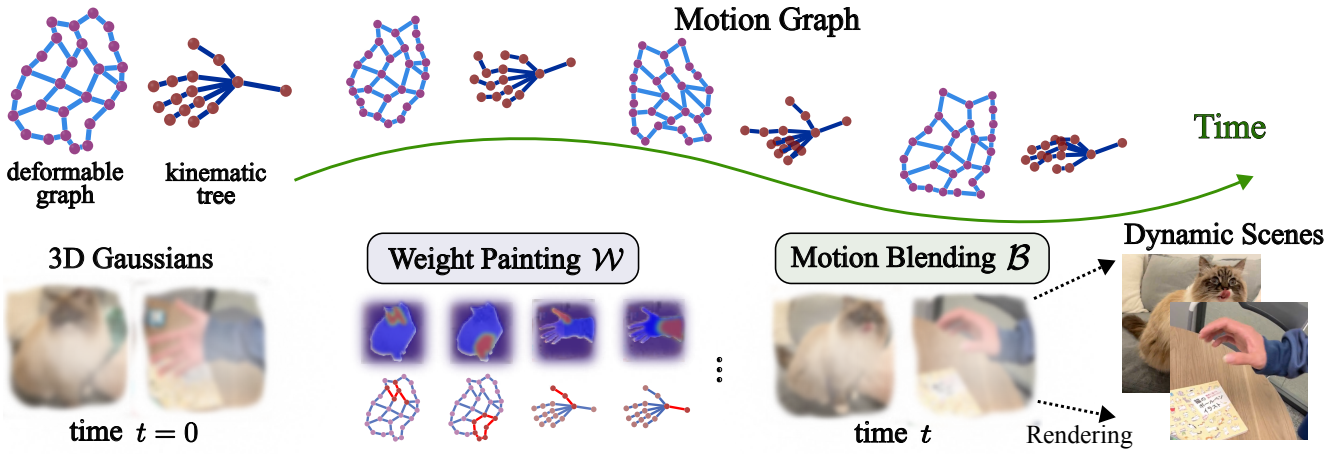


Figure 2. **Motion Blender Gaussian Splatting.** Our framework explicitly represents motion using sparse graph structures. Static 3D Gaussians are associated with dynamic motion graphs by learnable weight painting. Then, link-wise motions are propagated to Gaussians through motion blending with dual quaternion skinning. We introduce two motion graph types: kinematic trees, ideal for capturing articulated structures like human bodies, and deformable graphs, designed for modeling non-rigid deformations in soft objects. The parameters of the motion graph, weight painting functions, and 3D Gaussians are jointly optimized end-to-end via differentiable rendering.

Gaussian $g \in \mathcal{G}$ is parameterized by its pose $\mathbf{p} \in \mathrm{SE}(3)$, scale $\mathbf{s} \in \mathbb{R}^3$, opacity $o \in \mathbb{R}$ and color $\mathbf{c} \in \mathbb{R}^3$. 2D images can be rendered from $\mathcal{G}$ by blending the colors of overlapping Gaussians along the ray direction of each pixel.

Dynamic Gaussian splatting extends each Gaussian by making it time-dependent, g_t, where $t \in [0, T-1]$ and T represents the number of frames in the source video. The common practice is to make the pose time-dependent, $\mathbf{p}_t$, and keep the rest static. $\mathbf{p}_t$ is often obtained from a model f as in Eq. 1, where θ denotes the model's parameters.

$$\mathbf{p}_t = f(\mathbf{p}_0, t; \theta), \text{where } t > 0 \tag{1}$$

Function f is often implemented as a neural net such as a deformation field network [46, 48], or as a shallow model such as motion coefficients or polynomials [24, 25, 44] that require per-Gaussian motion parameters.

3.1. Motion Blender Gaussian Splatting

Our motion blender framework is designed based on two key ideas that set it apart from existing methods. 1 Represent motions with a sparse structure: Instead of associating dense motion parameters to each Gaussian (often numbering in the hundreds of thousands), we use a motion graph with far fewer parameters (often less than 100). The sparse link-wise motions are then propagated to each Gaussian through motion blending. 2 Represent motions explicitly: Instead of encoding motions implicitly into neural networks, our motion graph provides an explicit motion representation. This allows a straightforward visualization and manipulation of motions in the 3D space, such as transferring motion patterns from one object to a new object, or creating novel animations through motion graph editing.

Formally, we define the motion graph $G_t = (\mathcal{J}_t, \mathcal{L})$ at time t as a set of joints $\mathcal{J}_t$ with a set of edges $\mathcal{L}$, where $\max(|\mathcal{J}_t|, |\mathcal{L}|) \ll |\mathcal{G}|$. Each link $l \in \mathcal{L}$ is defined as $l = (s_l, e_l)$ and consists of the start and end joint indexes $s_l, e_l \in [1, J]$. The positions of all the links at time t are arranged as a matrix $X_{\mathcal{L},t} \in \mathbb{R}^{|\mathcal{L}| \times 6}$, where each row corresponds to the 3D coordinates of the start and end joints for a link in $\mathcal{L}$. Similarly, $\mathbf{x}_t \in \mathbb{R}^3$ denotes the position of a Gaussian with pose $\mathbf{p}_t$ at time t. We assume both the edges $\mathcal{L}$ and the number of joints $|\mathcal{J}_t|$ stay static, and only joint positions undergo motions over time. Let $P_{\mathcal{L},t} \in \mathrm{SE}(3)^{|\mathcal{L}|}$ be the poses of all the links at time t. Let $\mathbf{p}_0$ be the parameter that describes the initial pose of a Gaussian, then $\mathbf{p}_t$ is given by Eq. 2.

$$\mathbf{p}_t = \mathcal{B}\big(\mathcal{R}\left(P_{\mathcal{L},0}, P_{\mathcal{L},t}\right), \mathcal{W}\left(\mathbf{x}_0, X_{\mathcal{L},0}\right)\big) \cdot \mathbf{p}_0 \tag{2}$$

$\mathcal{W} : \mathbb{R}^3 \times \mathbb{R}^{L \times 6} \mapsto \Delta^{L-1}$ denotes the *weight painting function*, where Δ^{L-1} represents the probability vector space defined as $\{\mathbf{w} \in \mathbb{R}_+^L \mid \sum_{i=1}^L \mathbf{w}_i = 1\}$. This function $\mathcal{W}$ estimates the influence of each link $l \in \mathcal{L}$ to a given Gaussian based on their relative positions at $t = 0$.

$\mathcal{R} : \mathrm{SE}(3)^L \times \mathrm{SE}(3)^L \mapsto \mathrm{SE}(3)^L$ computes the relative rigid transformations between two sets of 3D poses. Specifically, $\mathcal{R}\left(P_{\mathcal{L},0}, P_{\mathcal{L},t}\right)$ captures the link-wise SE(3) movements from time 0 to time t.

$\mathcal{B} : \mathrm{SE}(3)^L \times \Delta^{L-1} \mapsto \mathrm{SE}(3)$ represents the *motion blending function*, which computes the per-Gaussian motion by propagating the link-wise movements $\mathcal{R}\left(P_{\mathcal{L},0}, P_{\mathcal{L},t}\right)$ to each Gaussian based on the weights assigned by $\mathcal{W}$ at $t = 0$.

We implement $\mathcal{B}$ using dual quaternion skinning

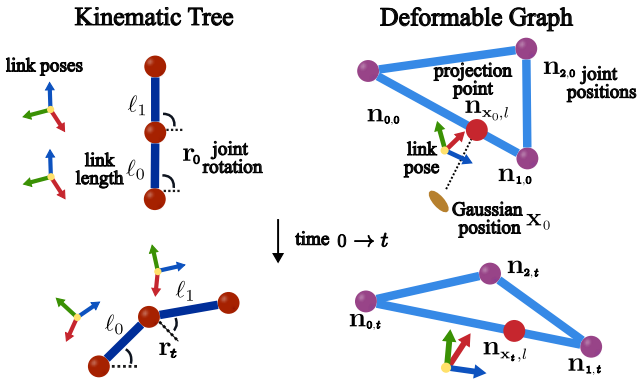


Figure 3. **Motion Graphs.** A kinematic tree (left) uses time-independent link lengths ℓ and dynamic joint rotations $\mathbf{r}_t \in \mathrm{SO}(3)$. Link poses (shown as colored coordinate axes) are computed through forward kinematics. A deformable graph (right) employs free-form topology parameterized by joint positions $\{\mathbf{n}_{i,t}\}$ and has non-rigid link deformations. Rigid per-link poses are obtained relative to each Gaussian position $\mathbf{x}_0$ and look-at transformation as in Eq. 3 and Eq. 4.

(DQS) [16]. DQS represents transformations using dual quaternions and computes weighted averages in a way that guarantees the resulting transformation remains valid in SE(3) space. The link-wise movements computed by $\mathcal{R}$ are analytically determined, as the relative SE(3) transformation can be straightforwardly derived. Therefore, our motion blender framework hinges on two key design choices: (1) Modeling graph motions by representing their temporal evolution through link poses $P_{\mathcal{L},t}$. (2) Defining a weight painting function $\mathcal{W}$ that accurately captures the influence of each graph link on a Gaussian's motion. We address the former design choice by presenting two types of parametric motion graphs in Sec. 3.2. The latter, the design of $\mathcal{W}$, is detailed in Sec. 3.3. The overall motion blender gaussian splatting framework is visualized in Fig. 2.

3.2. Motion Graph Representation

To predict link poses $P_{\mathcal{L},t}$, we represent them as a parameterized function $\mathcal{P}_{\mathcal{L}}(\theta, \phi) \in \mathrm{SE}(3)^L$. Here, θ encodes the graph parameters that determine the configuration of link poses at a given instant, and ϕ encodes the time-independent graph parameters. By modeling θ as a time-varying sequence $(\theta_t)_{t=0}^{T-1}$, the link poses at time t are defined as $P_{\mathcal{L},t} = \mathcal{P}_{\mathcal{L}}(\theta_t, \phi)$, where θ_t governs the kinematic state of the graph at time t. Two types of motion graphs, kinematic trees and deformable graph, are shown in Fig. 3.

Kinematic Tree. A kinematic tree is a hierarchical, acyclic graph with a root joint. This representation is ideal for capturing the kinematic chains of articulated objects such as human bodies, robot arms, or other multi-joint systems. We parameterize the tree using $\theta = (\mathbf{r}, \mathbf{X}), \phi = (\ell_i)_{i=1}^{L}$, where $\ell_i \in \mathbb{R}^+$ denotes the length of the i-th link, $\mathbf{r} \in \mathrm{SO}(3)^J$ represents the joint rotations, with J denoting the number of joints, and $\mathbf{X} \in \mathrm{SE}(3)$ denotes the pose of the root joint. The $\mathcal{P}_{\mathcal{L}}(\theta_t, \phi)$ can be implemented via a forward kinematics algorithm [21], which propagates transformations from the root node through the tree, compounding rotations and translations across joints to derive every link pose. The forward kinematic procedure is differentiable, which enables the learning of θ and ϕ through back-propagation.

Deformable Graph. Unlike the kinematic tree, a deformable graph imposes no topological constraints, allowing joints to move freely in 3D space. This representation is ideal for modeling non-rigid deformations and surface variations in soft objects. We parameterize the graph as $\theta = (\mathbf{n}_j \in \mathbb{R}^3)_{j=1}^{J}, \phi = ()$, where $\mathbf{n}_j$ denotes the 3D position of the j-th joint. However, the absence of topological constraints allows links between joints to stretch or compress, making it impossible to describe link poses $\mathcal{P}_{\mathcal{L}}(\theta, \phi)$ using rigid transformations. To address this, we redefine the link pose as $P_{\mathcal{L}}(\theta, \mathbf{x})$, relative to a reference viewpoint $\mathbf{x}$. In practice, the position of each Gaussian is used as the reference viewpoint. For each link l with start joint $\mathbf{n}_{s_l,0}$ and end joint $\mathbf{n}_{e_l,0}$ at $t = 0$, we define $\mathbf{n}_{\mathbf{x}_0,l} \in \mathbb{R}^3$ as the point on l that has the minimal distance to $\mathbf{x}_0$. We refer $\mathbf{n}_{\mathbf{x}_0,l}$ as the projection point at $t = 0$. Next, we define the projection point $\mathbf{n}_{\mathbf{x}_t,l}$ at time t in Eq. 3.

$$\mathbf{n}_{\mathbf{x}_t,l} = \mathbf{n}_{s_l,t} + \frac{|\mathbf{n}_{\mathbf{x}_0,l} - \mathbf{n}_{s_l,0}|}{|\mathbf{n}_{s_l,0} - \mathbf{n}_{e_l,0}|}(\mathbf{n}_{s_l,t} - \mathbf{n}_{e_l,t}) \quad (3)$$

In other words, the projection point $\mathbf{n}_{\mathbf{x}_t,l}$ moves proportionally to the stretching of link l. Next, the link pose $P_{\mathcal{L}}(\theta_t, \mathbf{x}_t)$ is derived via look-at transformation in Eq. 4.

$$P_{\mathcal{L}}(\theta_t, \mathbf{x}_t) = \{\mathscr{A}(\mathbf{n}_{\mathbf{x}_t,l}, \mathrm{ray}(\mathbf{n}_{s_l,t}, \mathbf{n}_{e_l,t})), \forall l \in \mathcal{L}\} \quad (4)$$

where $\mathrm{ray}(\mathbf{a}, \mathbf{b}) = \frac{\mathbf{b}-\mathbf{a}}{|\mathbf{b}-\mathbf{a}|}$ is the unit direction vector from $\mathbf{a}$ to $\mathbf{b}$. The look-at transformation $\mathscr{A} : \mathbb{R}^3 \times S^2 \mapsto \mathrm{SE}(3)$ maps the viewing position and direction to a SE(3) pose [40]. Note that look-at transformation requires defining an up-direction for each link. We organize the L links into $\frac{L}{2}$ triangles and use their face normals as up-directions. Remark that there is a key distinction between our deformable graph and the deformation graph used in DynamicFusion [29]. DynamicFusion attaches SE(3) poses directly to joints only. Our method represents each joint as a $\mathbb{R}^3$ position, which simplifies motion-graph editing, and derives SE(3) link poses from joints. The link poses are then used to construct Gaussian motions.

Graph Connectivity $\mathcal{L}$ Initialization. The last problem to address is determining the graph connectivity $\mathcal{L}$, which defines the links between joints as integer pairs $l = (s_l, e_l)$,



Figure 4. **Learned Motion Graphs and Weight Paintings.** The first row overlays the learned motion graphs on the rendered images. The second row visualizes the painted weights (red) of the specific graph links (green).

where $s_l, e_l \in [1, J]$ denote the indices of the start and end joints. The connectivity $\mathcal{L}$ is treated as a fixed parameter, neither receiving gradients nor changing over time. For kinematic trees, connectivity is derived from domain-specific priors, such as lifting 2D human skeletons to 3D or extracting from robot models. For deformable graphs, we initialize $\mathcal{L}$ by randomly sampling and connecting points from a point cloud, using farthest point sampling [6] to ensure uniform coverage of the object's surface, as illustrated in Fig. 6 and detailed in Sec. 3.4.

3.3. Weight Painting Function

To estimate the influence of each graph link on a Gaussian, we represent the weight painting function as: $\mathcal{W}(\mathbf{x}_0, X_{\mathcal{L},0}) = \text{softmax}(\{K(\mathbf{x}_0, X_{\mathcal{L},0,i}) \mid \forall i \in [1, L]\})$, where $\mathbf{x}_0$ denotes the initial position of a Gaussian, and $X_{\mathcal{L},0,i} \in \mathbb{R}^6$ represents the initial positions of the start and end joints of the i-th link. The kernel function $K_\psi : \mathbb{R}^3 \times \mathbb{R}^6 \to \mathbb{R}$, measures the affinity between a Gaussian and a link. We define the kernel as:

$$K(\mathbf{x}_0, X_{\mathcal{L},0,i}) = \exp\left(-\gamma \cdot \text{dist}(\mathbf{x}_0, X_{\mathcal{L},0,i})\right) \tag{5}$$

where γ is a learnable parameter that controls the kernel radius. By learning distinct γ at each link, the motion graph's influence regions collectively span the object's surface. At $t = 0$, 3D Gaussians reconstruct the objects' initial geometry. The static reconstruction is bonded to the dynamic motion graph through weight painting. The painted weights are subsequently used to propagate motions for $t > 0$ to achieve dynamic reconstruction.

3.4. Optimization Details

To reconstruct dynamic scenes from videos, we follow common practices [29, 44] and select the frame where objects occupy the largest image area as the canonical frame instead of using the first frame. For simplicity, we still use $t = 0$ to denote canonical frame. We extract instance segmentation masks using Grounding SAM2 [14, 19, 26, 36–38] and 2D human skeletons using SAPIENS [18]. These annotations are used to initialize the motion graph for each instance at the canonical frame. Specifically, the motion graph is parameterized by $(\theta_t)_{t=0}^{T-1}$ (time-varying parameters) and ϕ (time-independent parameters). We create the graph for each instance at the canonical frame with (θ_0, ϕ) and propagate the parameters across time by setting $\theta_t = \theta_0, \forall t \in [0, T-1]$. We illustrate the motion graph initialization procedure for the canonical frame in Fig. 6. The 3D Gaussians are initialized for every instance and background using procedure from prior work [44]. At each iteration, we transform the 3D Gaussians from the canonical frame $t = 0$ to a target frame t using Eq. 2, and minimize the rendering loss against the corresponding video frame.

Instance Level Reconstruction. To reconstruct each instance, we construct a binary matrix $M \in \mathbb{R}^{|\mathcal{G}| \times I}$, where $|\mathcal{G}|$ denotes the number of Gaussians and I denotes the number of instances. M is defined in Eq. 6.

$$M_{ij} = \begin{cases} 1 & i\text{-th Gaussian belongs to instance } j \\ 0 & \text{otherwise} \end{cases} \tag{6}$$

The i-th row of M represents the one-hot encoding of the instance index for each Gaussian. We then splat M into a 2D instance mask of dimension $\mathbb{R}^{H \times W \times I}$ and minimize the L1 distance between this rendered mask and the instance mask predicted by Grounding SAM2. In doing so, 3D positions of Gaussians are grouped to faithfully represent the geometry of each instance, as illustrated in Fig. 10.

Canonical Frame Regularization. To ensure the learned motion graph remains closely aligned with the object geometry, we minimizes $\sum_{i=1}^{J} \|\mathbf{n}_{i,0} - \hat{\mathbf{n}}_{i,0}\|$ during training, where $\mathbf{n}_{i,0}$ denotes the position of the current i-th joint at the canonical frame, and $\hat{\mathbf{n}}_{i,0}$ represents the position of the same joint but before training. This regularization ensures that the motion graph, which is initialized close to the object geometry prior training, does not drift away from the object during optimization.

2D Keypoints Regularization. We project the 3D joints of

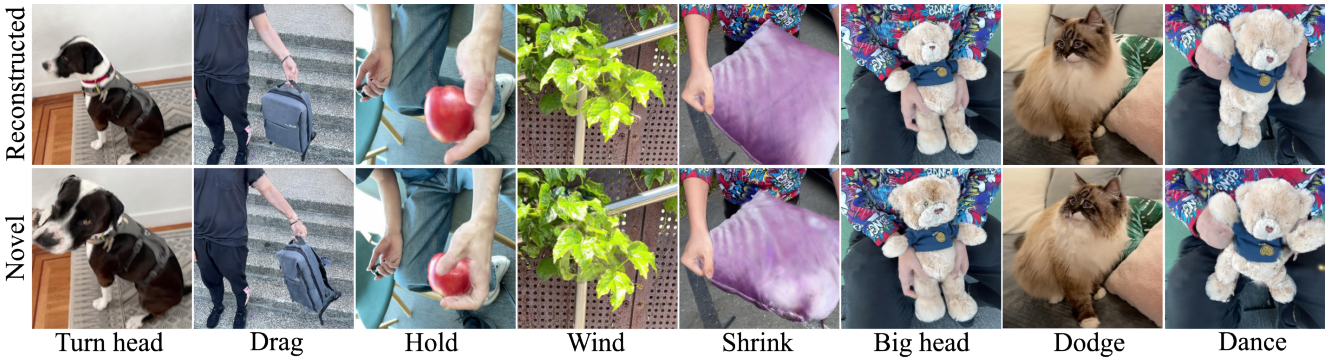


Figure 5. **Novel Poses from Motion Graph Editing.** The first row shows the observed scene rendered from reconstructed Gaussians. By editing motion graphs and propagating changes to the Gaussians, we create novel, unseen poses, as rendered in the second row.

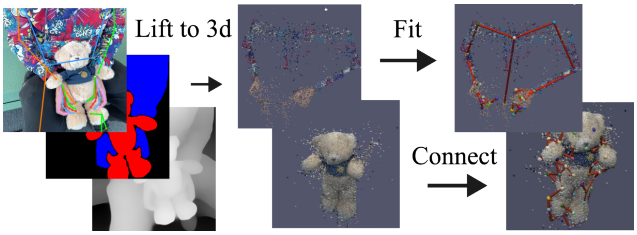


Figure 6. **Motion Graph Initialization.** At $t = 0$, we lift 2D skeletons and instance masks to 3D point clouds using depth images. For kinematic structures such as the human body, we leverage prior knowledge of joint connections to initialize a kinematic tree with standard joint rotations and link lengths. This tree is then fitted to the point cloud skeleton by minimizing the average point-to-link distance via gradient descent. For deformable graphs, we sample points from the instance point cloud using farthest point sampling [6] and connect adjacent points to form the graph.

the human kinematic tree onto the image plane and minimize the L1 distance between the projected joint positions and the 2D human keypoints predicted by SAPIENS.

4. Experiment

Sec. 4.1 introduces our experimental settings. In Sec. 4.2, we compare our results with SoTA Gaussian splatting methods on real-world datasets. We then show two applications of our method: creating novel object poses and synthesizing robot demonstrations. Finally, we conduct ablation studies in Sec. 4.4 and discuss the limitations in Sec. 4.5.

4.1. Settings

Datasets. We evaluate our method on two real-world datasets: the iPhone dataset [8] from [44] and the HyperNeRF [32] vrig dataset. The iPhone dataset consists of 12 scenes, including 5 multi-camera (MV) and 7 single-camera (SV) scenes, each captured at 960×720 resolution. The MV scenes are captured using one hand-held moving camera and two fixed cameras at novel angles, where the hand-held video is used for training and the fixed cameras for quantitative evaluation. The SV scenes, captured solely with a hand-held camera, are used for qualitative visualization. The HyperNeRF vrig dataset consists of 4 scenes, each captured at 960×540 resolution using two cameras mounted on a rig kit with strong camera motions. Models are trained on a subset of frames and evaluated on the remaining frames.

Table 1. Quantitative results for novel view rendering on iPhone dataset. LPIPS more accurately reflects perceptual quality.

Method	LPIPS ↓	PSNR ↑	SSIM ↑
T-NeRF [8]	0.55	15.6	0.55
HyperNeRF [32]	0.51	15.99	0.59
DynIBaR [23]	0.55	13.41	0.48
Deformable-GS [48]	0.66	11.92	0.49
4DGaussians [46]	0.561	13.42	0.49
Shape-of-Motion [44]	0.39	16.67	**0.65**
Ours	**0.37**	**16.79**	**0.65**

Baselines. On the iPhone dataset, we compare against Shape-of-Motion [44]. For HyperNeRF, we compare against 4DGaussians [46]. Both represent the SoTA on their respective datasets. Following Shape-of-Motion, we use their proposed 2D track loss in addition to L1 rgb loss.

Metrics. We report peak-signal-to-noise ratio (PSNR), structural similarity index (SSIM) [45] and learned perceptual image patch similarity (LPIPS) [51]. Since traditional metrics such as PSNR and SSIM are sensitive to minor misalignments and often favor blurry images over sharp ones [32], we adopt LPIPS as our primary metric.

4.2. Results

Tab. 1 presents our quantitative results on the iPhone benchmark, where our method outperforms the state-of-the-art Shape-of-Motion by 0.02 LPIPS. Fig. 7 provides a qualitative comparison on the five MV scenes with 4DGaus-

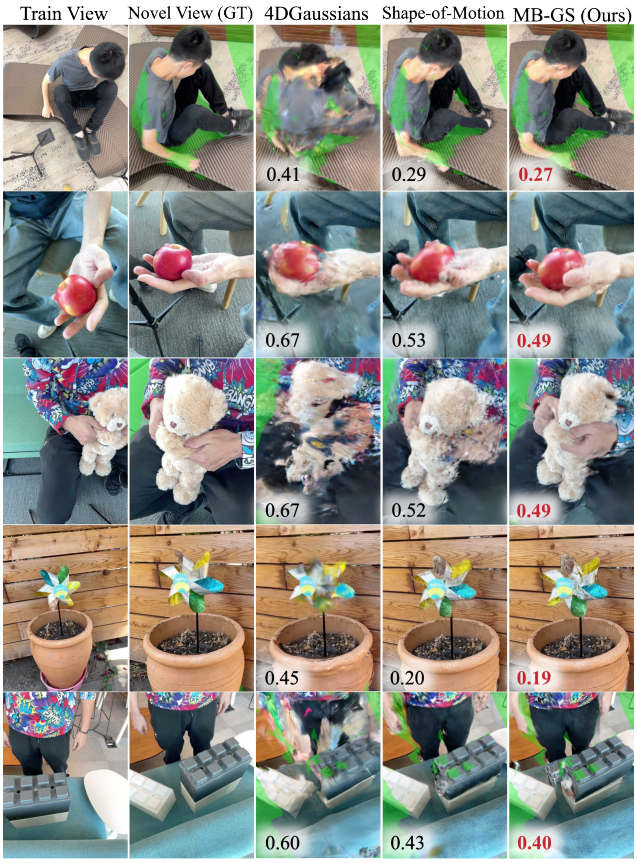


Figure 7. Visualization of novel view rendering on iPhone dataset compared with other methods. Regions in green are excluded from evaluation, as these pixels are never seen in training videos. LPIPS on bottom left with best colored red.

Table 2. Quantitative results on HyperNerf dataset. Our method performs competitively, closely matching SoTAs in LPIPS.

	LPIPS ↓	PSNR ↑	SSIM ↑
4DGaussians [46]	0.36	**25.19**	**0.68**
Shape-of-Motion [44]	**0.34**	21.01	0.54
Ours	0.35	20.60	0.54

sians [46] and Shape-of-Motion [44], demonstrating that our method renders sharper, more complete, and perceptually higher-quality novel views. While 4DGaussians achieves comparable PSNR and SSIM scores, its rendering quality is notably inferior. Fig. 4 visualizes the learned motion graphs and weight paintings. Training on the iPhone dataset converges within 10 to 30 hours on a 40GB A100 GPU, depending on scene complexity. For the teddy bear scene with 2M Gaussians—using a deformable graph for the bear and a kinematic tree for the human—our method achieves a rendering speed of 18 FPS, and 25 FPS if motion

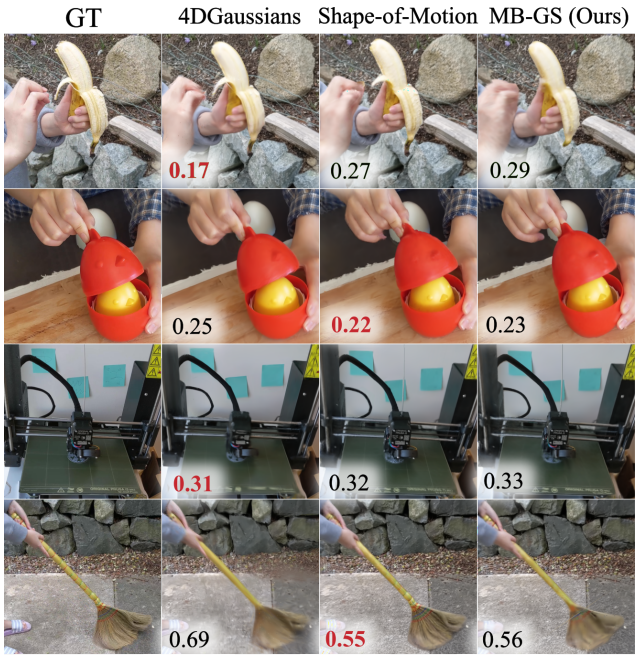


Figure 8. Visualization of results in HyperNerf dataset compared with other methods. LPIPS on bottom left with best colored red.

graphs for each frame are pre-computed and cached. On smaller scenes, such as the chicken toy in HyperNeRF with 300K Gaussians, the rendering speed increases to 32 FPS without caching and 46 FPS with caching.

Tab. 2 presents our quantitative results on the HyperNeRF vrig benchmark, with qualitative comparison across four scenes in Fig. 8. While 4DGaussians, the SoTA on HyperNeRF, achieves higher PSNR and SSIM, our method achieves a comparable or better rendering quality and LPIPS on the chicken, 3D printer, and broom scenes (rows 2 to 4 in Fig. 8). Notably, 4DGaussians achieves a better LPIPS score on the 3D printer scene, but our method produces clearer results, accurately rendering the text on the printer motor, unlike the blurry output from 4DGaussians. However, on the peel-banana scene, our method produces lower-quality results than 4DGaussian. We further discuss our limitations in Sec. 4.5.

4.3. Applications

Novel Pose Animation. Fig. 5 shows images of objects in novel poses that were not seen in the training videos. After reconstructing dynamic scenes, we keep the Gaussians fixed and modify the motion graph starting from a sampled frame. Specifically, we adjust joint rotation angles in a kinematic tree or manipulate the positions of subsets of joints in a deformable graph. These edits are performed interactively using a custom visual editor that we built on VISER [10]. Once the edits are applied, we propagate the updated graph link poses to the Gaussians and render

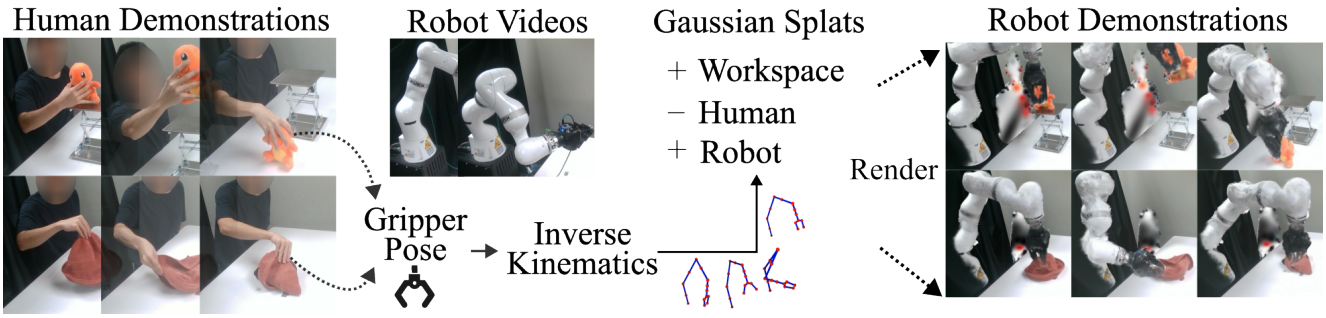


Figure 9. **Robot Demonstration from Human Videos.** We reconstruct Gaussians from human and robot videos, with the robot's pre-defined kinematic chain as the motion graph. We then remove Gaussians of the human and add robot's to workspace. Next, we animate the robot motion graph using inverse kinematics derived from the hand pose. This renders videos of a robot arm mimicking human actions.

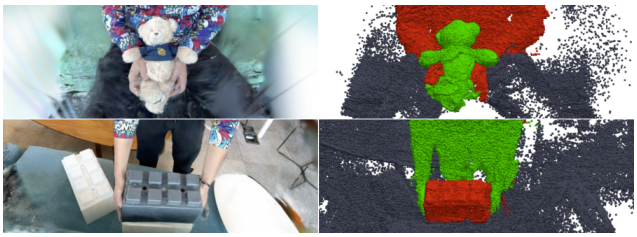


Figure 10. Visualization of rendered scene (left) and underlying Gaussian positions as point cloud (right). The point cloud is colored to distinguish individual instances and background.

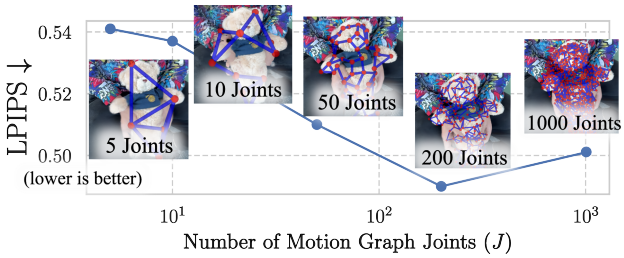


Figure 11. Relationship between novel view rendering quality and motion graph size.

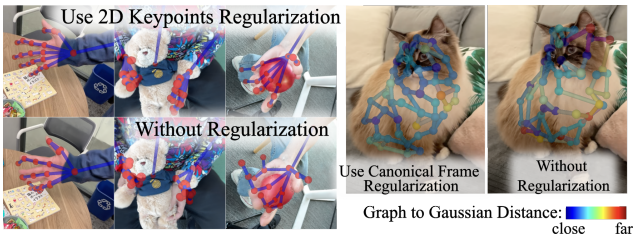


Figure 12. Visualization of rendered images and motion graphs with and without 2D human keypoint regularization (left) and canonical frame regularization (right).

the scene from the same camera viewpoint as the sampled frame. To create short animations, we interpolate joint angle or position changes incrementally and render the scene frame-by-frame.

Fig. 5 shows that our method extends beyond reconstructing observed motions, enabling the creation of novel object motions while maintaining high rendering quality. Recent advances in controllable image and video editing predominantly rely on large diffusion models [2, 11, 41]. In contrast, our method introduces a novel approach by operating directly in 3D space, enabling precise control over object poses without the need for neural networks.

Robot Demonstration Synthesis. Imitation learning enables robots to perform complex tasks by learning from robot demonstrations. Unlike human videos, collecting robot demonstrations requires labor-intensive teleoperation. In Fig. 9, we demonstrate a prototype of our method for synthesizing robot demonstrations from human videos.

We reconstruct scenes from human and robot videos independently. For robot videos, we use the pre-defined robot kinematic chain as the motion graph, available from the robot system runtime. We then remove the human Gaussians and add robot Gaussians to the workspace. Keyframes are manually selected, with hand positions mapped to robot gripper poses using our visual editor. Gripper poses between keyframes are interpolated, and inverse kinematics converts them into joint angles of the robot kinematic chain. The chain is then used as the robot motion graph for view rendering. This generates a video where the robot replaces the human, completing the task as demonstrated. While artifacts and unrealistic interactions still present, this demonstrates the potential of our approach for robotic applications.

4.4. Ablation Studies

Motion Graph Size. Fig. 11 illustrates the relationship between novel view rendering quality and the number of joints in a motion graph. We observe that the best rendering quality for the teddy scene is achieved with a motion graph of 200 joints. However, increasing the number of joints to

1000 leads to a noticeable drop in quality, suggesting the existence of an optimal graph size. This finding highlights the potential of learning adaptive graph structures that dynamically adjust to different objects.

2D Keypoints Regularization. Fig. 12 compares rendered images and motion graphs with and without 2D human keypoint regularization. We observe that enforcing consistency between the projected 3D kinematic tree and 2D human keypoints (detected by SAPIENS [18]) improves performance, reducing LPIPS by 0.01 to 0.02. More importantly, this regularization produces cleaner and more meaningful motion graphs that align well with the human 3D structure. Without 2D keypoint regularization, the motion graph tends to drift or produce suboptimal structures. For example, if two fingers move together, the kinematic tree may incorrectly control both with a single finger link, leaving other finger links static. This highlights the importance of 2D keypoint regularization in learning accurate and interpretable 3D motion graphs.

Canonical Frame Regularization. The right side of Fig. 12 compares rendered images and motion graphs with and without canonical frame regularization, which minimizes the distance between the learned motion graph's joint positions and their initial positions at the canonical frame. The joints and links of the motion graph are color-coded based on their distance to the Gaussians on the object surface. With canonical frame regularization, the motion graph remains closely aligned with the object surface. Without it, however, the graph joints become spiky (indicated by red-colored joints) and drift outward, detaching from the object.

4.5. Limitations

Fig. 13 illustrates examples of imperfectly learned motion graphs and a failure case in motion editing. Despite using 2D human keypoint regularization, learning precise and complex kinematic trees for small regions remains challenging. For instance, in the left image, the hand—which contains intricate kinematic structures—occupies a small region (less than 80×80 pixels in a 720×920 image), making it difficult to capture fine details. Additionally, the learning of deformable graphs heavily depends on the quality of the canonical frame's point cloud. Noisy point clouds can lead to suboptimal initializations, such as joints placed outside the object or incomplete coverage of certain object parts, as shown in the middle example. Further, the right example demonstrates a failure case in motion editing, where attempting to turn the cat's head introduces non-negligible visual artifacts. Unlike meshes, Gaussians lack an explicit surface representation, allowing them to deform arbitrarily when motion graphs are applied. This can result in unrealistic deformations, especially for motions not present in the training videos.



Figure 13. Visualization of imperfect learned motion graphs (left, middle) and a failure case in motion editing (right).

In addition to the limitations in Fig. 13, our method produces inferior rendering quality on certain HyperNeRF scenes. HyperNerf scenes are captured with strong rotating camera motions, where objects frequently enter and exit the scene, which is deemed unrealistic by [8]. 4DGaussians addresses this challenge by employing a deformation field network, allowing all Gaussians to move freely. In contrast, our method does not use neural networks and learns motion graph parameters directly at each frame, making it less adaptable to rapid camera motions. A promising direction is to integrate a deformation network into the motion graph framework, predicting motion graph parameters instead of learning them as free variables, enhancing adaptability while preserving interpretability.

5. Conclusion

We introduced Motion Blender Gaussian Splatting (MB-GS), a framework for dynamic scene reconstruction using explicit and sparse motion graphs. MB-GS achieves state-of-the-art performance on the iPhone dataset and competitive results on HyperNeRF. We demonstrate its applications in novel pose animation and synthesizing robot demonstrations from human videos. We hope our work can be useful for future research in dynamic scene reconstruction, robotics, and animation.

References

[1] Ang Cao and Justin Johnson. Hexplane: A fast representation for dynamic scenes. In *Proceedings of the IEEE/CVF Conference on Computer Vision and Pattern Recognition*, pages 130–141, 2023. 2

[2] Duygu Ceylan, Chun-Hao P Huang, and Niloy J Mitra. Pix2video: Video editing using image diffusion. In *Proceedings of the IEEE/CVF International Conference on Computer Vision*, pages 23206–23217, 2023. 8

[3] Haonan Chang and Abdeslam Boularias. Scene-level tracking and reconstruction without object priors. *2022 IEEE/RSJ International Conference on Intelligent Robots and Systems (IROS)*, pages 3785–3792, 2022. 2

[4] Haonan Chang, Dhruv Metha Ramesh, Shijie Geng, Yuqiu Gan, and Abdeslam Boularias. Mono-star: Mono-camera scene-level tracking and reconstruction. *2023 IEEE International Conference on Robotics and Automation (ICRA)*, pages 820–826, 2023. 2

[5] Blender Online Community. *Blender - a 3D modelling and rendering package*. Blender Foundation, Stichting Blender Foundation, Amsterdam, 2018. 2

[6] Yuval Eldar, Michael Lindenbaum, Moshe Porat, and Yehoshua Y Zeevi. The farthest point strategy for progressive image sampling. *IEEE transactions on image processing*, 6(9):1305–1315, 1997. 5, 6

[7] Sara Fridovich-Keil, Giacomo Meanti, Frederik Rahbæk Warburg, Benjamin Recht, and Angjoo Kanazawa. K-planes: Explicit radiance fields in space, time, and appearance. In *Proceedings of the IEEE/CVF Conference on Computer Vision and Pattern Recognition (CVPR)*, pages 12479–12488, 2023. 2

[8] Hang Gao, Ruilong Li, Shubham Tulsiani, Bryan Russell, and Angjoo Kanazawa. Monocular dynamic view synthesis: A reality check. *Advances in Neural Information Processing Systems*, 35:33768–33780, 2022. 2, 6, 9

[9] Wei Gao and Russ Tedrake. Surfelwarp: Efficient non-volumetric single view dynamic reconstruction, 2019. 2

[10] NeRF Studio Group. Viser: Web-based 3d visualization + python. https://github.com/nerfstudio-project/viser, 2023. 7

[11] Yi Huang, Jiancheng Huang, Yifan Liu, Mingfu Yan, Jiaxi Lv, Jianzhuang Liu, Wei Xiong, He Zhang, Shifeng Chen, and Liangliang Cao. Diffusion model-based image editing: A survey. *arXiv preprint arXiv:2402.17525*, 2024. 8

[12] Yi-Hua Huang, Yang-Tian Sun, Ziyi Yang, Xiaoyang Lyu, Yan-Pei Cao, and Xiaojuan Qi. Sc-gs: Sparse-controlled gaussian splatting for editable dynamic scenes. In *Proceedings of the IEEE/CVF Conference on Computer Vision and Pattern Recognition (CVPR)*, pages 4220–4230, 2024. 1, 2

[13] Doug L James and Christopher D Twigg. Skinning mesh animations. *ACM Transactions on Graphics (TOG)*, 24(3): 399–407, 2005. 2

[14] Qing Jiang, Feng Li, Zhaoyang Zeng, Tianhe Ren, Shilong Liu, and Lei Zhang. T-rex2: Towards generic object detection via text-visual prompt synergy, 2024. 5

[15] Pushkar Joshi, Mark Meyer, Tony DeRose, Brian Green, and Tom Sanocki. Harmonic coordinates for character articulation. *ACM transactions on graphics (TOG)*, 26(3):71–es, 2007. 2

[16] Ladislav Kavan, Steven Collins, Jiří Žára, and Carol O'Sullivan. Skinning with dual quaternions. In *Proceedings of the 2007 symposium on Interactive 3D graphics and games*, pages 39–46, 2007. 2, 4

[17] Bernhard Kerbl, Georgios Kopanas, Thomas Leimkühler, and George Drettakis. 3d gaussian splatting for real-time radiance field rendering. *ACM Trans. Graph.*, 42(4):139–1, 2023. 1, 2

[18] Rawal Khirodkar, Timur Bagautdinov, Julieta Martinez, Su Zhaoen, Austin James, Peter Selednik, Stuart Anderson, and Shunsuke Saito. Sapiens: Foundation for human vision models. *arXiv preprint arXiv:2408.12569*, 2024. 5, 9

[19] Alexander Kirillov, Eric Mintun, Nikhila Ravi, Hanzi Mao, Chloe Rolland, Laura Gustafson, Tete Xiao, Spencer Whitehead, Alexander C. Berg, Wan-Yen Lo, Piotr Dollár, and Ross Girshick. Segment anything. *arXiv:2304.02643*, 2023. 5

[20] Tianshu Kuai, Akash Karthikeyan, Yash Kant, Ashkan Mirzaei, and Igor Gilitschenski. Camm: Building category-agnostic and animatable 3d models from monocular videos. In *Proceedings of the IEEE/CVF Conference on Computer Vision and Pattern Recognition*, pages 6587–6597, 2023. 2

[21] Serdar Kucuk and Zafer Bingul. *Robot kinematics: Forward and inverse kinematics*. INTECH Open Access Publisher London, UK, 2006. 4

[22] Zhe Li, Yipengjing Sun, Zerong Zheng, Lizhen Wang, Shengping Zhang, and Yebin Liu. Animatable and relightable gaussians for high-fidelity human avatar modeling. *arXiv preprint arXiv:2311.16096*, 2023. 2

[23] Zhengqi Li, Qianqian Wang, Forrester Cole, Richard Tucker, and Noah Snavely. Dynibar: Neural dynamic image-based rendering. In *Proceedings of the IEEE/CVF Conference on Computer Vision and Pattern Recognition*, pages 4273–4284, 2023. 6

[24] Zhan Li, Zhang Chen, Zhong Li, and Yi Xu. Spacetime gaussian feature splatting for real-time dynamic view synthesis. In *Proceedings of the IEEE/CVF Conference on Computer Vision and Pattern Recognition*, pages 8508–8520, 2024. 1, 2, 3

[25] Youtian Lin, Zuozhuo Dai, Siyu Zhu, and Yao Yao. Gaussian-flow: 4d reconstruction with dynamic 3d gaussian particle. In *Proceedings of the IEEE/CVF Conference on Computer Vision and Pattern Recognition*, pages 21136–21145, 2024. 2, 3

[26] Shilong Liu, Zhaoyang Zeng, Tianhe Ren, Feng Li, Hao Zhang, Jie Yang, Chunyuan Li, Jianwei Yang, Hang Su, Jun Zhu, et al. Grounding dino: Marrying dino with grounded pre-training for open-set object detection. *arXiv preprint arXiv:2303.05499*, 2023. 5

[27] Matthew Loper, Naureen Mahmood, Javier Romero, Gerard Pons-Moll, and Michael J Black. Smpl: A skinned multi-person linear model. In *Seminal Graphics Papers: Pushing the Boundaries, Volume 2*, pages 851–866. 2023. 2

[28] Ben Mildenhall, Pratul P Srinivasan, Matthew Tancik, Jonathan T Barron, Ravi Ramamoorthi, and Ren Ng. Nerf: Representing scenes as neural radiance fields for view synthesis. *Communications of the ACM*, 65(1):99–106, 2021. 2

[29] Richard A Newcombe, Dieter Fox, and Steven M Seitz. Dynamicfusion: Reconstruction and tracking of non-rigid scenes in real-time. In *Proceedings of the IEEE conference on computer vision and pattern recognition*, pages 343–352, 2015. 2, 4, 5

[30] Jesús R Nieto and Antonio Susín. Cage based deformations: a survey. In *Deformation Models: Tracking, Animation and Applications*, pages 75–99. Springer, 2012. 2

[31] Keunhong Park, Utkarsh Sinha, Jonathan T. Barron, Sofien Bouaziz, Dan B Goldman, Steven M. Seitz, and Ricardo Martin-Brualla. Nerfies: Deformable neural radiance fields. In *Proceedings of the IEEE/CVF International Conference on Computer Vision (ICCV)*, pages 5865–5874, 2021. 2

[32] Keunhong Park, Utkarsh Sinha, Peter Hedman, Jonathan T Barron, Sofien Bouaziz, Dan B Goldman, Ricardo Martin-Brualla, and Steven M Seitz. Hypernerf: A higher-

dimensional representation for topologically varying neural radiance fields. *arXiv preprint arXiv:2106.13228*, 2021. 2, 6

[33] Hanspeter Pfister, Matthias Zwicker, Jeroen Van Baar, and Markus Gross. Surfels: Surface elements as rendering primitives. In *Proceedings of the 27th annual conference on Computer graphics and interactive techniques*, pages 335–342, 2000. 2

[34] Albert Pumarola, Enric Corona, Gerard Pons-Moll, and Francesc Moreno-Noguer. D-nerf: Neural radiance fields for dynamic scenes. In *Proceedings of the IEEE/CVF Conference on Computer Vision and Pattern Recognition (CVPR)*, pages 10318–10327, 2021. 2

[35] Zhiyin Qian, Shaofei Wang, Marko Mihajlovic, Andreas Geiger, and Siyu Tang. 3dgs-avatar: Animatable avatars via deformable 3d gaussian splatting. In *Proceedings of the IEEE/CVF conference on computer vision and pattern recognition*, pages 5020–5030, 2024. 2

[36] Nikhila Ravi, Valentin Gabeur, Yuan-Ting Hu, Ronghang Hu, Chaitanya Ryali, Tengyu Ma, Haitham Khedr, Roman Rädle, Chloe Rolland, Laura Gustafson, Eric Mintun, Junting Pan, Kalyan Vasudev Alwala, Nicolas Carion, Chao-Yuan Wu, Ross Girshick, Piotr Dollár, and Christoph Feichtenhofer. Sam 2: Segment anything in images and videos, 2024. 5

[37] Tianhe Ren, Qing Jiang, Shilong Liu, Zhaoyang Zeng, Wenlong Liu, Han Gao, Hongjie Huang, Zhengyu Ma, Xiaoke Jiang, Yihao Chen, Yuda Xiong, Hao Zhang, Feng Li, Peijun Tang, Kent Yu, and Lei Zhang. Grounding dino 1.5: Advance the "edge" of open-set object detection, 2024.

[38] Tianhe Ren, Shilong Liu, Ailing Zeng, Jing Lin, Kunchang Li, He Cao, Jiayu Chen, Xinyu Huang, Yukang Chen, Feng Yan, Zhaoyang Zeng, Hao Zhang, Feng Li, Jie Yang, Hongyang Li, Qing Jiang, and Lei Zhang. Grounded sam: Assembling open-world models for diverse visual tasks, 2024. 5

[39] Taha Samavati and Mohsen Soryani. Deep learning-based 3d reconstruction: a survey. *Artificial Intelligence Review*, 56(9):9175–9219, 2023. 2

[40] Scratchapixel. Framing: The look-at function. https://www.scratchapixel.com/lessons/mathematics-physics-for-computer-graphics/lookat-function/framing-lookat-function.html, 2025. Accessed: 2025-02-20. 4

[41] Yujun Shi, Chuhui Xue, Jun Hao Liew, Jiachun Pan, Hanshu Yan, Wenqing Zhang, Vincent YF Tan, and Song Bai. Dragdiffusion: Harnessing diffusion models for interactive point-based image editing. In *Proceedings of the IEEE/CVF Conference on Computer Vision and Pattern Recognition*, pages 8839–8849, 2024. 8

[42] Robert W Sumner, Johannes Schmid, and Mark Pauly. Embedded deformation for shape manipulation. In *ACM siggraph 2007 papers*, pages 80–es. 2007. 2

[43] Homer Rich Walke, Kevin Black, Tony Z. Zhao, Quan Vuong, Chongyi Zheng, Philippe Hansen-Estruch, Andre Wang He, Vivek Myers, Moo Jin Kim, Max Du, Abraham Lee, Kuan Fang, Chelsea Finn, and Sergey Levine. Bridgedata v2: A dataset for robot learning at scale. In *Proceedings of The 7th Conference on Robot Learning*, pages 1723–1736. PMLR, 2023. 2

[44] Qianqian Wang, Vickie Ye, Hang Gao, Jake Austin, Zhengqi Li, and Angjoo Kanazawa. Shape of motion: 4d reconstruction from a single video. *arXiv preprint arXiv:2407.13764*, 2024. 1, 2, 3, 5, 6, 7

[45] Zhou Wang, Alan C Bovik, Hamid R Sheikh, and Eero P Simoncelli. Image quality assessment: from error visibility to structural similarity. *IEEE transactions on image processing*, 13(4):600–612, 2004. 6

[46] Guanjun Wu, Taoran Yi, Jiemin Fang, Lingxi Xie, Xiaopeng Zhang, Wei Wei, Wenyu Liu, Qi Tian, and Xinggang Wang. 4d gaussian splatting for real-time dynamic scene rendering. In *Proceedings of the IEEE/CVF conference on computer vision and pattern recognition*, pages 20310–20320, 2024. 1, 2, 3, 6, 7

[47] Tianyi Xie, Zeshun Zong, Yuxing Qiu, Xuan Li, Yutao Feng, Yin Yang, and Chenfanfu Jiang. Physgaussian: Physics-integrated 3d gaussians for generative dynamics. In *Proceedings of the IEEE/CVF Conference on Computer Vision and Pattern Recognition*, pages 4389–4398, 2024. 1, 2

[48] Ziyi Yang, Xinyu Gao, Wenming Zhou, Shaohui Jiao, Yuqing Zhang, and Xiaogang Jin. Deformable 3d gaussians for high-fidelity monocular dynamic scene reconstruction. *2024 IEEE/CVF Conference on Computer Vision and Pattern Recognition (CVPR)*, pages 20331–20341, 2023. 1, 2, 3, 6

[49] Zeyu Yang, Hongye Yang, Zijie Pan, and Li Zhang. Real-time photorealistic dynamic scene representation and rendering with 4d gaussian splatting. *arXiv preprint arXiv:2310.10642*, 2023. 1, 2

[50] Ye Yuan, Xueting Li, Yangyi Huang, Shalini De Mello, Koki Nagano, Jan Kautz, and Umar Iqbal. Gavatar: Animatable 3d gaussian avatars with implicit mesh learning. In *Proceedings of the IEEE/CVF Conference on Computer Vision and Pattern Recognition*, pages 896–905, 2024. 2

[51] Richard Zhang, Phillip Isola, Alexei A Efros, Eli Shechtman, and Oliver Wang. The unreasonable effectiveness of deep features as a perceptual metric. In *Proceedings of the IEEE conference on computer vision and pattern recognition*, pages 586–595, 2018. 6

[52] Linglong Zhou, Guoxin Wu, Yunbo Zuo, Xuanyu Chen, and Hongle Hu. A comprehensive review of vision-based 3d reconstruction methods. *Sensors*, 24(7):2314, 2024. 2